Climate Dynamics (2018) 51:2229–2246
https://doi.org/10.1007/s00382-017-4009-y

Interdecadal change in the summer SST-precipitation relationship around the late 1990s over the South China Sea

Jiepeng Chen[1] · Xin Wang[1,2] · Wen Zhou[3] · Zhiping Wen[4]

Received: 14 March 2017 / Accepted: 8 November 2017 / Published online: 18 November 2017

Abstract
An interdecadal change in the air-sea interaction over the South China Sea (SCS) after the late 1990s has been identified using a local contemporaneous precipitation-sea surface temperature (SST) and precipitation-SST tendency relationship. During 1979–1998, there is a negative precipitation-SST relationship over the SCS, with a larger magnitude over the northeastern SCS (NESCS) than over the southwestern SCS (SWSCS). The remote effect of warmer SST over the tropical Indian Ocean plays a crucial role in a strong anticyclone and suppressed rainfall over the SCS and western North Pacific. Due to greater mixed-layer depth over the SWSCS than over the NESCS, entrainment heat flux makes a larger contribution to a positive precipitation-SST tendency over the SWSCS than over the NESCS. The cloud-radiation effect has a dominant and positive contribution to the SST tendency over the NESCS, whereas it has a negative contribution to SST tendency over the SWSCS. In contrast, the precipitation-SST correlation becomes weakly negative over the NESCS and significantly positive over the SWSCS during 1999–2013. The CESM-CAM5 model demonstrates that cooler SST over the tropical central-eastern Pacific (TCEP) triggers a weak anticyclone, slightly suppressing rainfall over the SCS. The cloud-radiation effect still contributes mostly to a positive SST tendency over the NESCS. Warmer SST over the SWSCS induces an increase in surface evaporation and low-level moisture convergence and causes enhanced rainfall. That offsets the remote effect of TCEP SST and results in a negative precipitation-SST tendency with negative cloud-radiation feedback. The interdecadal change in remote forcing to SCS rainfall around the late 1990s is related to the evolution of TCEP SST anomalies from the preceding winter to summer, which is possibly modulated by the phase of the Pacific Decadal Oscillation.

Keywords South China Sea · Summer precipitation-SST relationship · Interdecadal change · Around the late 1990s

1 Introduction

The South China Sea (SCS) is the third largest continental marginal sea in the world after the Coral Sea and Arabian Sea (Groves and Hunt 1980), with an average depth of over 2000 m (Xie et al. 2003). The SCS links the Pacific Ocean and Indian Ocean and belongs to the Asian-Pacific monsoon region (Wang et al. 2009). A warmer sea surface temperature (SST) anomaly over the western Pacific warm pool from February to April is conducive to an early onset of the SCS summer monsoon (Liang et al. 2013). The reversal of the east–west SST gradient between the SCS and western North Pacific is favorable for eastward migration of the summer monsoon (Wu and Wang 2001; Wu 2002; Lau and Nath 2009). Not only do the underlying SST condition and associated heating over the SCS affect the local circulation environment, they also have a strong effect on the adjoining monsoon regions (He et al. 2016). The SCS also acts to transport moisture from the western North Pacific (WNP), the Southern Hemisphere, and the north Indian Ocean to East Asia (Zhou and Yu 2005; Li et al. 2011, 2014; Zhang et al. 2011; Chen et al. 2015a). Understanding the mechanisms of SCS

✉ Xin Wang
wangxin@scsio.ac.cn

[1] State Key Laboratory of Tropical Oceanography, South China Sea Institute of Oceanology, Chinese Academy of Sciences, Guangzhou 510301, China

[2] Laboratory for Regional Oceanography and Numerical Modeling, Qingdao National Laboratory for Marine Science and Technology, Qingdao, China

[3] Guy Carpenter Asia-Pacific Climate Impact Centre, School of Energy and Environment, City University of Hong Kong, Hong Kong SAR, China

[4] Institute of Atmospheric Sciences, Fudan University, Shanghai, China

air-sea interaction is a prerequisite for improving the predictability of the East Asian climate.

The contributions of atmospheric and oceanic processes to the SCS summer air-sea interaction have been indicated by previous research. After the onset of the SCS summer monsoon, due to the orographic effect of the Annam Cordillera, a strong southwesterly wind jet appears offshore east of Saigon and gives rise to a cold filament (10°–13°N, 110°–118°E) through a coastal upwelling mechanism, Ekman pumping on the northern flank of this wind jet, and an evaporative cooling effect. The cold filament refers to the eastward extension of cold surface water from the Vietnamese coast, which spreads northeastward and results in basin-wide cooling over the SCS in summer (Xie et al. 2003). He and Wu (2013) also indicate a wind-induced oceanic effect on SST tendency along the west coast and a dominant atmospheric forcing over the SCS with a cloud-radiation effect and wind-evaporation effect during April–May–June. It has been documented that variability in the SCS summer climate is influenced not only by local air-sea interaction but also by remote forcing. Many previous studies (e.g., Wang and Zhang 2002; Wang et al. 2006; Lau and Nath 2009) pointed out that ENSO exerts a remarkable impact on SCS climate variability. The influences of the central Pacific El Niño and eastern Pacific El Niño on SCS summer rainfall are noticeably different (Chen et al. 2014b). In addition, SST anomalies over the tropical Indian Ocean (Wu et al. 2010, 2012; He and Wu 2014; Chen et al. 2016), and tropical central-western Pacific (Chen et al. 2015a) play an important role in the multi-scale variability of SCS rainfall.

The local and simultaneous precipitation-SST relationship and precipitation-SST tendency can be used to distinguish the SST forcing of the atmosphere from the atmospheric forcing of SST (Wu et al. 2006; Wu and Kirtman 2007). Due to relatively fast atmospheric responses to SST anomalies, positive (negative) SST anomalies could cause an increase (decrease) in rainfall through enhanced (reduced) low-level moisture convergence, surface evaporation, and thermal convection. This local dominant influence of SST on rainfall is reflected in a positive precipitation-SST correlation, which is typical of the equatorial central-eastern Pacific throughout the year, in the southeast Indian Ocean in summer and winter, and in the WNP in winter (Wu and Kirtman 2007). With above-normal (below-normal) rainfall, a decrease (increase) in incoming shortwave radiation because of enhanced (reduced) cloudiness makes a large contribution to a negative (positive) SST tendency. This is the case over the WNP in summer and over the southeast Indian Ocean in January-March. It features negative precipitation-SST and precipitation-SST tendency correlations, which indicates atmospheric feedback. Except for the cloud-radiation effect, the wind-evaporation effect and wind-induced oceanic mixing and upwelling can contribute to the SST change (Wu and Kirtman 2007; He and Wu 2013). The local and simultaneous SST-precipitation correlation on a seasonal timescale is generally important for understanding seasonal prediction skill of rainfall (Kumar et al. 2013). In tropical-subtropical regions where SST-rainfall correlation is highly positive, SST becomes a driver of the local rainfall variability. Then the slowly varying oceanic condition that affects the SST anomalies becomes a potential source of high seasonal rainfall prediction skill in those regions.

In boreal summer, there is a significant positive precipitation-SST relationship over most regions of the tropical Indian Ocean and Pacific Ocean, as shown in Fig. 1a, while there are negative correlations between precipitation and underlying SST over the western Pacific, eastern SCS, and the Bay of Bengal as revealed by previous studies (e.g., Wang et al. 2005; Wu et al. 2009; Lu and Lu 2014). It is noted that a weak positive precipitation-SST relationship appears over the western SCS. Previous studies (Gadgil et al. 1984; Graham and Barnett 1987; Rajendran et al. 2012) suggested the relationship between SST and organized deep convection is non-linear over tropical ocean, when SST is above the threshold in the vicinity of 27.5–28 °C. The tropical mean SST warming after the late 1990s could raise the SST threshold conducive to convection itself (Johnson and Xie 2010). This study indicates that the summer precipitation-SST correlation over the SCS experiences a remarkable interdecadal change around the late 1990s (Fig. 1b–e). This raises the question, what are the differences in the air-sea interaction process over the SCS in summer before and after the late 1990s? The anomalies in the upper ocean heat content (0–400m) in the SCS changed from negative to positive after the late 1990s (Fig. 2 in Song et al. 2014). Meanwhile, the eastward jet shifted southward associated with the southern SCS anticyclone and northern SCS cyclonic ocean gyres (Wang et al. 2010). Moreover, there is a positive to negative phase transition of the Pacific Decadal Oscillation (PDO) around the late 1990s, which changes the summer precipitation pattern in East China through the air-sea interaction (Zhu et al. 2011, 2015) and strengthens the relationship with tropical Pacific-North Pacific SST variability (Jo et al. 2015). What are the local and remote factors that resulted in the interdecadal change in the precipitation-SST relationship after the late 1990s? These issues will be investigated in the present study.

The rest of this study is organized as follows. Section 2 describes the datasets, methods, and model used. Section 3 provides the interdecadal characteristics of the simultaneous summer precipitation-SST correlation. The air-sea interaction processes over the SCS for the periods 1979–1998 and 1999–2013 are explored in Sects. 4 and 5, respectively. The reasons for the interdecadal change in the air-sea interaction over the SCS are discussed in Sect. 6. Finally, a summary and discussion are given in Sect. 7.

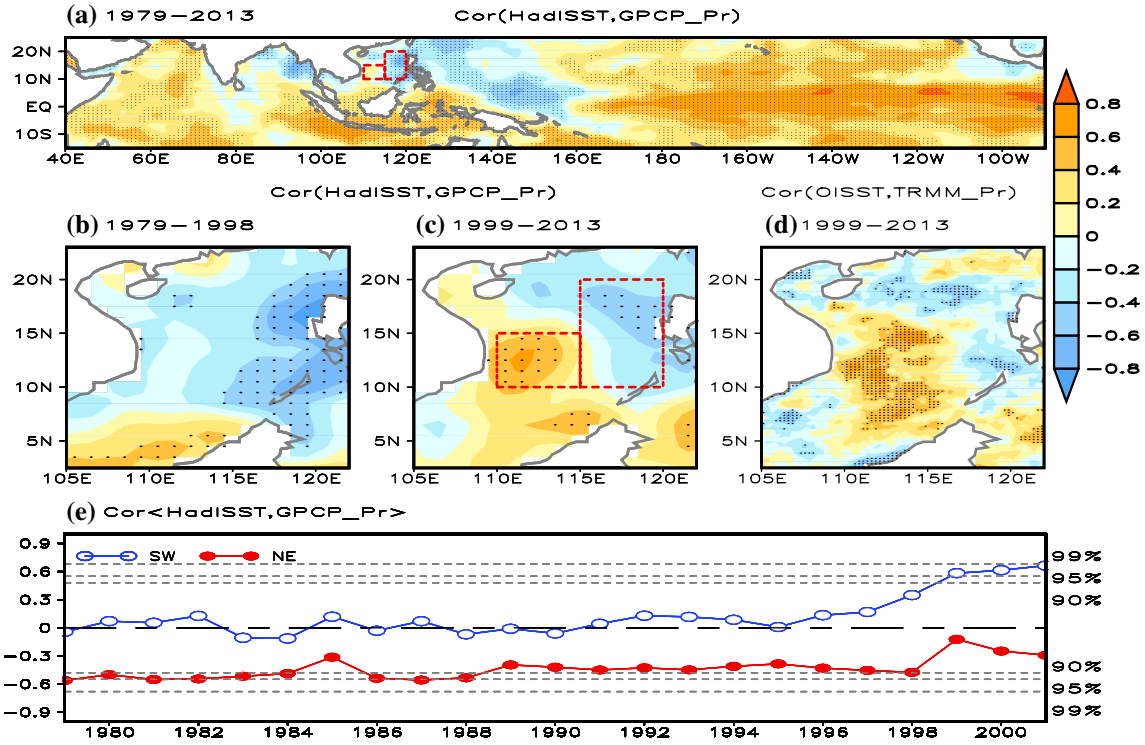

Fig. 1 Point-wise and simultaneous JJA-mean SST-precipitation correlation for the periods 1979–2013 (**a**), 1979–1998 (**b**), and 1999–2013 (**c, d**), respectively. **e** simultaneous 13-year moving SST-precipitation correlation for the period 1979–2013 averaged over the region 10°–15°N and 110°–115°E (SWSCS, blue line) and 10°–20°N and 115°-120°E (NESCS, red line), which are indicated with rectangles in **a** and **c**. The correlation coefficient is shown for the first year of the 13-year window. The dots **a**–**d** indicate correlation coefficients that are statistically significant at the 90% confidence level. Precipitation data are derived from GPCP version 2 (**a**–**c, e**) and TRMM (**d**). SST data are obtained from HadISST (**a**–**c, e**) and OISST (**d**)

2 Datasets, methods, and model

2.1 Datasets

Precipitation datasets used in this study include (1) monthly mean precipitation starting from January 1979 derived from the Global Precipitation Climatology Project (GPCP; Adler et al. 2003), which combines observations and satellite precipitation data into 2.5° × 2.5° global grids; (2) monthly mean CPC Merged Analysis of Precipitation (CMAP; Xie and Arkin 1997) at a 2.5°×2.5° resolution from 1979 to the present, provided by NOAA/OAR/ESRL PSD, Boulder, Colorado, USA; (3) daily precipitation from ERA-Interim at a 1.5° × 1.5° resolution from 1979 to the present, provided by the European Centre for Medium-Range Weather Forecasts (ECMWF); and (4) 3-hour precipitation from the Tropical Rainfall Measuring Mission (TRMM) 3B42 product on 0.25° × 0.25° grids since December 1997, obtained from the Goddard Earth Sciences Data and Information Services Center, National Aeronautics and Space Administration (NASA).

The present study adopts three SST datasets, including (1) monthly NOAA Extended Reconstruction SST in version 3b (NOAA_ERSST_V3; Smith et al. 2008), derived from ICOADS with a resolution of 2°×2° from 1854 to the present, which can be downloaded from http://www.esrl.noaa.gov/psd/data/gridded/data.noaa.ersst.html; (2) monthly Hadley Centre sea ice and SST (HadISST; Rayner et al. 2003), obtained from Met Office Hadley Centre observation datasets and available on 1° × 1° grids starting from January 1870; (3) daily NOAA High Resolution SST (OISST; Reynolds et al. 2007) on 0.25° × 0.25° grids since September 1981, provided by NOAA/OAR/ESRL PSD and available from http://www.esrl.noaa.gov/psd/data/gridded/data.noaa.oisst.v2.highres.html.

Monthly vertical velocity, geopotential height, winds, temperature, and special humidity are derived from the Japanese 55-year Reanalysis project (JRA-55; Kobayashi et al. 2015). The JRA-55 dataset is available on 1.25° × 1.25° grids from 1958 to the present, which is maintained by the Japan Meteorological Agency (JMA) and can be downloaded from http://jra.kishou.go.jp/index.html.

Monthly shortwave radiation, longwave radiation, sensible heat flux, and latent heat flux data provided by JRA-55 are also used in this study. As a parallel analysis, this study employs the TropFlux dataset (Kumar et al. 2012), which is

available on 1° × 1° grids within 30°S × 30°N from January 1979 to about 4 months before the present. The TropFlux dataset can be obtained from http://www.incois.gov.in/tropflux_datasets/data/monthly/. Note that positive values of surface heat flux denote downward flux and thus would cause warming of the ocean mixed layer, and vice versa. Most descriptions in the text refer to results based on the JRA-55 data. The use of TropFlux data is noted where it occurs. Monthly wind stress, sea surface height, and ocean subsurface temperature are obtained from the simple ocean data assimilation (SODA2.2.4) ocean reanalysis from 1979 to 2010 on a grid of 0.5° latitude × 0.5° longitude. The climatological monthly Sea-viewing Wide Field-of-view Sensor (SeaWiFS) Level-3 Mapped Chlorophyll Data in version 2014 (Hu et al. 2012) is used, which is provided by NASA Ocean Biology Distributed Active Archive Center (OB.DAAC), Goddard Space Flight Center, Greenbelt, MD, USA and downloaded from https://oceandata.sci.gsfc.nasa.gov/SeaWiFS/Binned/Monthly_Climatology/CHL/. The SeaWiFS chlorophyll data is available from September 1997 to December 2010 on 9-km × 9-km grids.

2.2 Methods

To illustrate the role of atmospheric and oceanic processes in generating SST anomalies, a mixed-layer heat budget equation (formula 1; Wang et al. 2006; Dong et al. 2007) is analyzed.

$$\frac{\partial T_m}{\partial t} = \frac{\mathrm{SW} - \mathrm{SW_{pen}} + \mathrm{LW} + \mathrm{LH} + \mathrm{SH}}{\rho C_p h_m} + \left(\vec{U}_g + \vec{U}_e\right)\nabla T_m - \frac{W_e \cdot \Delta T}{h_m}. \quad (1)$$

The net surface heat flux (Q_{net}) is the sum of the net shortwave radiation, penetrative shortwave radiation flux (SW_{pen}), net longwave radiation (LW), latent heat flux (LH), and sensible heat flux (SH), which is positive into the ocean. h_m is the mixed-layer depth, which is defined as the depth at which the change in temperature from the surface temperature equals 0.5 °C, referred to Levitus (1982). ρ(1027 kg m^{-3}) is the density of seawater, C_p(4000 J kg^{-1} K^{-1}) is the specific heat of seawater at constant pressure, $\overrightarrow{U_g} = -g\nabla\eta \times \vec{k}/f$ is the geostrophic velocity vector, η is the sea surface height, $\overrightarrow{U_e} = (\vec{\tau} \times \vec{k})/(\rho f h_m)$ is the Ekman velocity vector, $\vec{\tau}$ is the wind stress, $W_e = Curl(\vec{\tau}/\rho f)$ is the Ekman pumping velocity, and ΔT is the difference in the ocean temperature between the mixed layer and just below the mixed layer. T_m is the mixed-layer temperature and can be well represented by SST in the SCS (He and Wu 2013). Thus, T_m on the left side of the equation is replaced by SST. The summer SST tendency is calculated as the difference between the JJA-mean and AMJ-mean SST.

Penetrative shortwave radiation flux (SW_{pen}) is estimated following the solar radiation penetration parameterization scheme (Paulson and Simpson 1977), $\mathrm{SW_{pen}} = \mathrm{SW} \times (1 - \mathrm{R})e^{-h_m/L}$ where R = 0.58 is the fraction of incident sunlight (mainly red and infrared) absorbed within the upper 2 m of the water column, L = 23 m is the attenuation depth for clear water. Considering the influences of nutrients and chlorophyll in the sea water (Thangaprakash et al. 2016), the attenuation depth is estimated as $L = 1/(0.027 + (0.0518 \times \mathrm{chlorophyll}^{0.428}))$ (Morel 1988). The climatological summer mean in chlorophyll averaged over 108°–120°E and 10°–20°N in the period of 1998–2010 is 0.15 mg/m^3. The calculated result of the attenuation depth according to the above formula is equal to 20 m over SCS in summer. Thus, in this study penetrative shortwave radiation flux is estimated as 10% of shortwave radiation below mixed layer depth of 30 m and the attenuation depth of 20 m.

To calculate the pointwise and simultaneous SST-precipitation correlation, the precipitation data from GPCP and CMAP have been converted using linear interpolation into 1° × 1° grids and 2° × 2° grids, respectively. Empirical orthogonal function (EOF) analysis is used to extract the dominant spatial patterns of the variables and their evolution. The coordinated variation of precipitation and SST over the SCS is examined using the combined EOF.

2.3 Model experiments

To detect the influences of underlying SST anomalies on circulation and rainfall, atmospheric component CAM version 5 (CAM5) of the community Earth System Model (CESM) version 1.0.6 is adopted. CAM5 has been improved substantially in physical processes such as the moist turbulence scheme, shallow convection scheme, cloud macrophysics scheme, and so on (Neal et al. 2012). Three simulations are conducted at a horizontal resolution roughly equivalent to 1.25° longtitude × 0.9° latitude. The control experiment, referred to as EXP_CNL, is forced by the observed climatological mean seasonal cycle of global SST with a 22-year integration. The other two sensitivity experiments are similar to EXP_CNL, except that the regressed SST anomalies (shown in Figs. 4b, 8b) multiplied by 2 are imposed on the climatological SST over the tropical Indian Ocean (40°–100°E, 10°S–10°N) only (referred to as EXP_TIO) and over the tropical central-eastern Pacific (180°–80°W, 10°S–10°N) only (referred to as EXP_TCEP) in summer (Figs. 5, 9). The last 20-year ensemble mean outputs are analyzed in this paper, following Chen et al. (2014a, 2016).

3 Interdecadal change in the summer SST-precipitation relationship

The grid correlation coefficients between the JJA-mean SST and precipitation over the SCS for the period 1979–2013

based on GPCP precipitation and HadISST data are shown in Fig. 1a. Precipitation is significantly negatively correlated with the underlying SST variability over the eastern SCS. In contrast, the SST-precipitation correlation is very weak over the central-western SCS. A positive SST-precipitation correlation appears over the southern SCS. Apparently, the SST-precipitation correlation in the SCS north of 8°N is quite different from that south of 8°N. Moreover, the correlation in the SCS north of 8°N is not uniformly distributed in the west and east. Thus, the southwest SCS (SWSCS; 10°–15°N and 110°–115°E) and northeast SCS (NESCS; 10°–20°N and 115°–120°E) are selected to examine the interdecadal change in the SST-precipitation relationship in a comparative analysis. Thirteen-year moving correlation coefficients between SST and precipitation in summer for the period 1979–2013 over the SWSCS and NESCS are shown in Fig. 1e. The switch in the correlation over the SWSCS from weakly negative to significantly positive occurs in 1999. Meanwhile, a significant negative SST-precipitation correlation over the NESCS weakens after 1999. As shown in Table 1, the correlation coefficients during 1979–1998 are − 0.68 (− 0.62) in the NESCS, exceeding the 99% confidence level, and − 0.28 (− 0.39) in the SWSCS, based on GPCP precipitation and HadISST data (CMAP precipitation and ERSST data), respectively. The correlation coefficients during 1999–2013 are − 0.42 (− 0.073) in the NESCS and 0.49 (0.6) in the SWSCS at the 90% (95%) confidence level based on GPCP precipitation and HadISST data (CMAP precipitation and ERSST data), respectively. The absolute SST over the SCS is always above 28 °C. The climatological summer average of NESCS SST during 1979–2013 is greater than SWSCS SST by 0.26 °C. The difference in warming trend between NESCS and SWSCS is very small (0.01 °C per 10 years). That implies NESCS SST is more easily than SWSCS SST to reach at the SST threshold for deep convection. Once the SST threshold is crossed, organized convection is no longer dependent on the local SST. Scatter plot of absolute SST and rainfall in each grids over the southwestern SCS (Figure not shown) indicates local SST increase with a large spread in the rainfall values, manifesting a very weak negative SST-precipitation relationship during 1979–1998. During 1999–2013, the rainfall increases rapidly with SST up to around 29.5 °C, showing a strong positive SST-precipitation relationship. The results obtained in the present study are similar to Johnson and Xie (2010), who suggested the local SST threshold for deep convection increases along with the warming of the absolute mean local SST. Therefore, the periods 1979–1998 and 1999–2013 are selected as two sub-periods for contrasting analysis throughout this study.

Table 1 (a) Correlation coefficients over the NESCS (10°–20°N, 115°–120°E) and SWSCS (10°–15°N, 110°–115°E) for the periods 1979–1998 and 1999–2013 based on GPCP precipitation and HadISST data

(a) Correlation coefficient	NESCS	SWSCS
1979–1998	− 0.68 (99%)	− 0.28
1999–2013	− 0.42	0.49 (90%)
(b) Correlation coefficient	NESCS	SWSCS
1979–1998	− 0.62 (99%)	− 0.39
1999–2013	− 0.073	0.6 (95%)

(b) The same as (a) except for precipitation-SST correlations based on CMAP precipitation and ERSST data

For 1979–1998, a negative SST-precipitation correlation is observed in the SCS north of 8°N. The maximum centre appears in the NESCS (Fig. 1b). For 1999–2013, a significant positive SST-precipitation correlation is found in the SWSCS. The negative correlation can still be seen in the NESCS, but its scope narrows and its value decreases (Fig. 1c). When higher-resolution SST and precipitation data on 0.25° × 0.25° grids are used to calculate the SST-precipitation correlation for the period 1999–2013 (Fig. 1d), the distribution of the SST-precipitation correlation is consistent with those obtained from the other two datasets of precipitation and SST on 2° × 2° grids (figure not shown) and 1° × 1° grids (Fig. 1c), suggesting a robust finding. It is clear that the SST-precipitation correlation in the SCS is very different between 1979–1998 and 1999–2013, especially in the SWSCS, where it displays the opposite signal. This is the reason there is no obvious SST-precipitation correlation in the SWSCS for the whole period (1979–2013). Plausible factors that could impact the interdecadal change in the SST-precipitation correlation in the SCS after 1999 will be discussed in the following sections.

To investigate the co-variation of precipitation and SST over the SCS, both normalized precipitation and SST over the SCS are jointly subjected to a combined EOF analysis for the two sub-periods, separately. The first eigenmode accounts for 50.62 and 43.28% of the co-variance of rainfall and SST for the periods 1979–1998 and 1999–2013, respectively. During 1979–1998, the first eigenvector features the SCS basin modes with negative precipitation anomalies and positive SST anomalies (Fig. 2a), indicating a negative precipitation-SST relationship in a basin-wide pattern. During 1999–2013, the first spatial pattern of SST over the SCS exhibits unique warm anomalies. But for rainfall, its spatial pattern shows a northeast-southwest dipole with dry anomalies over the NESCS and enhanced rainfall over the SWSCS (Fig. 2c). Such a pattern illustrates that the co-variation of precipitation and SST over the SWSCS changes remarkably after 1999. The first principal components (PC1) for the two sub-periods contain noticeable interannual variations (Fig. 2b, d). It can be seen that the combined EOF analysis can capture a spatial phase relationship between

precipitation and SST over the SCS. The time series of SST anomalies over the NESCS and SWSCS show a synchronous change from 1979 to 2013, and the sign is the same. Precipitation variations over the NESCS and SWSCS show roughly the same change during 1979–1998 but an opposite change during 1999–2013. To further demonstrate the interdecadal change in the SCS precipitation pattern, the dominant precipitation patterns over the SCS are extracted by EOF analysis before and after 1999, respectively. The leading spatial pattern of summer rainfall over the region 0.5°S–21.5°N and 99.5°–120.5°E for the period 1979–2013 shows a north–south dipole along 10°N latitude, with suppressed rainfall in the south and enhanced rainfall in the north (Fig. 3a). The dominant spatial pattern during 1979–1998 is similar to that for the whole period, except that the loading over the SWSCS (10°–15°N and 110°–115°E) is larger than that for the whole period (Fig. 3c). However, during 1999–2013 the first spatial mode changes to an opposite-sign distribution in the northeast–southwest direction, accounting for more than 37% of the total variance (Fig. 3e). What is more, the interdecadal change in the dominant mode of precipitation over the SCS (Fig. 3c, e) is consistent with the coupled mode of precipitation with SST (Fig. 2a, c). Since dominant modes extracted by EOF analysis are sensitive to the domain, the first eigenvectors of global precipitation for the two sub-periods are calculated (figure not shown). The interdecadal change in the dominant mode of precipitation over the SCS can be represented in the first eigenvectors of precipitation in the global domain, except that their variances are smaller than the first eigenvectors of SCS precipitation.

4 Air-sea interaction over the SCS before 1999

To understand the cause of the interdecadal change in the air-sea interaction over the SCS, the influences of remote and local factors on the precipitation-SST relationship over the SCS in summer are explored. Figure 4 shows large-scale circulations related to the regulation of the SST and precipitation over the SCS during 1979–1998. Significant negative precipitation-positive SST anomalies appear in the SCS and east of the Philippines, while there is a positive relationship between local SST and precipitation in the tropical Indian Ocean (TIO) and the Maritime Continent. The warm SST anomalies in the TIO and the Maritime Continent could induce lower-level convergence, ascending motion, and upper-level divergence, according to Lindzen and Nigam (1987). The divergent winds flow from the TIO and converge over the SCS and WNP with winds from the equatorial eastern Pacific at 200 hPa. At 850 hPa, anomalous divergence is seen over the SCS and WNP, accompanying an anomalous descending motion and a positive SST tendency anomaly. An obvious anomalous anticyclone is located over the WNP and expands westward to the Bay of Bengal at 850 hPa, a stationary Kelvin wave response to positive SST anomalies over the TIO. Those result in divergence of water vapour flux vertically integrated from the sea surface to 300 hPa. The SST tendency anomalies in the TIO characterize a weak dipole mode with positive anomalies in the west and negative anomalies in the east, while the SST tendency anomalies in the equatorial central eastern Pacific are significant negative corresponding to an increase in rainfall. It is noted that

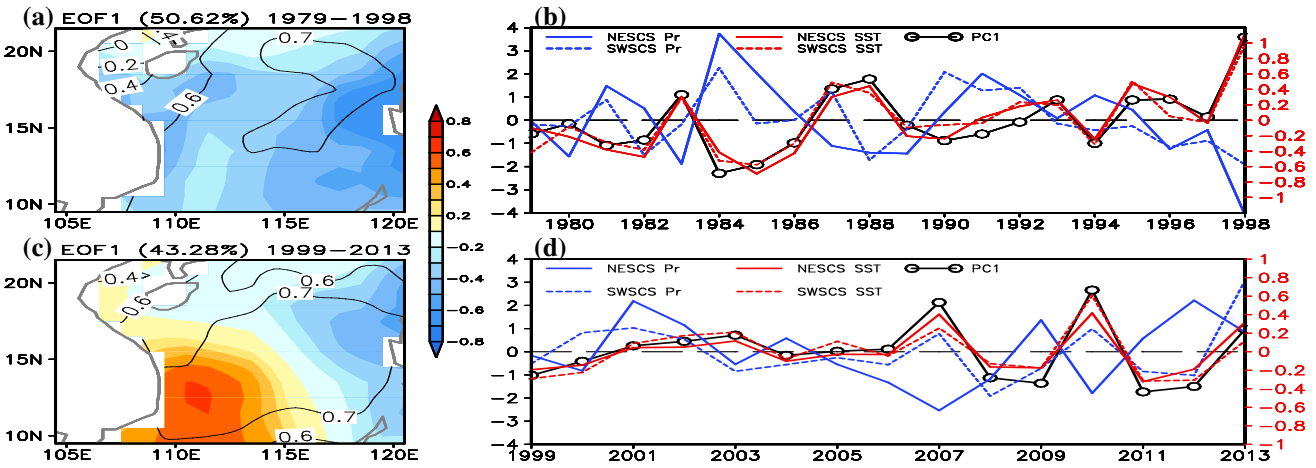

Fig. 2 The first eigenvector of the combined EOF modes of precipitation (shading) and SST (contours) in the SCS (9.5°–21.5°N, 104.5°–120.5°E) for the periods 1979–1998 (**a**) and 1999–2013 (**c**), and **b, d** their first principal components (PCs, solid lines with empty circles on left axes). The time series of precipitation anomalies (blue lines) and SST anomalies (red lines) over the NESCS (solid lines) and SWSCS (dashed lines) for the periods 1979–1998 (**b**) and 1999–2013 (**d**). Precipitation data are derived from GPCP version 2 and SST data are obtained from HadISST

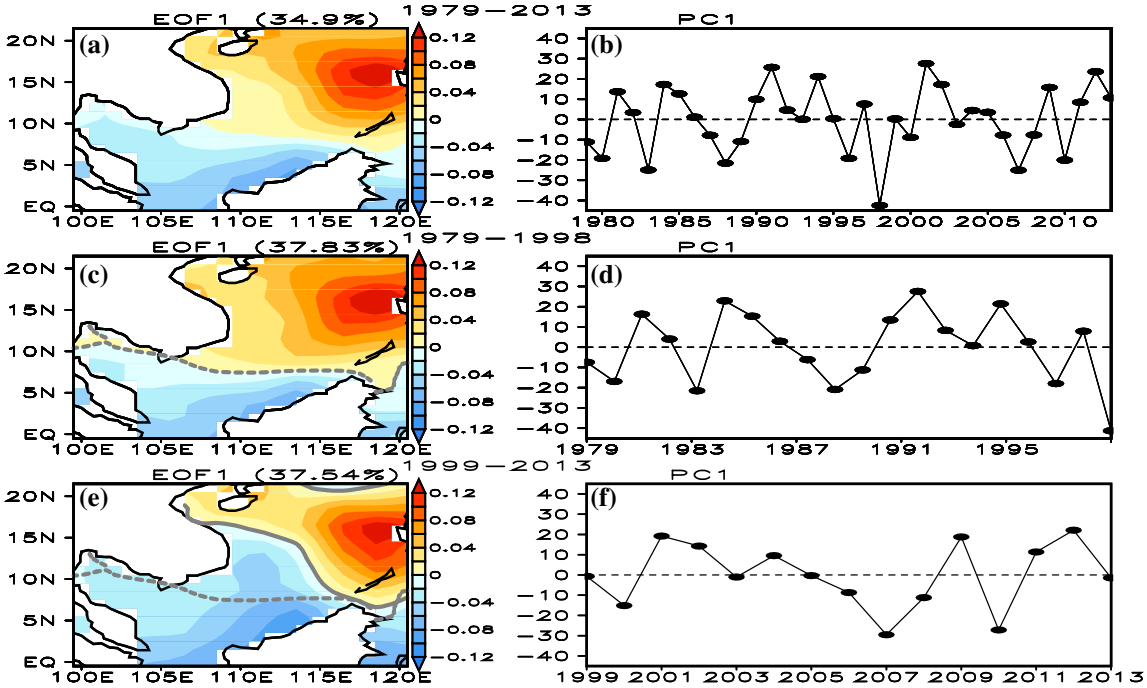

Fig. 3 The first eigenvectors of precipitation over the region 0.5°S–21.5°N and 99.5°–120.5°E (**a, c, e**) and their first PCs (**b, d, f**) for the periods 1979–2013 (**a, b**), 1979–1998 (**c, d**), and 1999–2013 (**e, f**), respectively. The gray dashed line and solid line highlight the zero value in the first eigenvector of precipitation during 1979–1998 and 1999–2013, respectively. GPCP precipitation data is used

in the TIO the magnitude of SST anomalies is larger than the SST tendency anomalies, whereas in the equatorial central eastern Pacific the magnitude of SST anomalies is smaller than the SST tendency anomalies. The warm SST anomalies in the TIO may contribute to a decrease in SCS summer rainfall, which is confirmed by the experiment EXP_TIO. Figure 5 shows the difference in the JJA-mean precipitation and 850 hPa winds between EXP_TIO and EXP_CNL. It is clear that an anomalous anticyclone and suppressed rainfall appear over the SCS and WNP in response to positive SST anomalies over the TIO.

The change in SST can be measured by the mixed-layer heat budget equation. The regressed anomalies of surface heat fluxes, geostrophic advection, Ekman advection, mixed-layer depth, and wind stress curl onto the normalized first PC of the combined EOF for the period 1979–1998 are shown in Fig. 6. More downward shortwave radiation shows a basin-wide pattern, corresponding to an anomalous anticyclone and suppressed rainfall. The surface net shortwave radiation anomalies are larger over the NESCS than the SWSCS, which shows a similar distribution of rainfall anomalies (Fig. 3c). The anomalies of longwave radiation, sensible heat flux, and latent heat flux are negative over the SWSCS and NESCS. Their magnitude is larger over the NESCS than the SWSCS but not for sensible heat flux anomalies. The center of sensible heat flux anomalies is located over the SWSCS and extends northeastward. Similar results are obtained using TropFlux data, except that the magnitude of surface heat fluxes is somewhat smaller compared to that based on the JRA-55 data. The contribution of surface heat flux to the SST tendency is associated with the variation in the mixed-layer depth. Significant positive anomalies of mixed-layer depth are located over the western SCS, while in the eastern SCS the mixed-layer depth is obviously negative. It is expected that surface heat flux anomalies within the deeper mixed layer will have less effect in inducing SST variation over the SWSCS than over the NESCS, which will be demonstrated in Fig. 7. The distribution of Ekman advections over the SCS shows a south–north oriented pattern with significant positive anomalies south of 12°N and negative anomalies north of 12°N. There is an obvious band of positive anomalies of geostrophic advections between 12°N and 17°N over the SCS. The anomalies of geostrophic advections over other regions have a scattered distribution. This implies that the contributions of Ekman advections and geostrophic advections to anomalously warmer SST over the SWSCS and NESCS are very small. The anomalous anticyclonic winds at 10 m over the SCS and the corresponding negative value of wind stress curl induce anomalous downward Ekman pumping velocity and may warm the mixed-layer SST.

To estimate quantitatively the contributions of surface heat fluxes and oceanic processes to SST anomalies over the SWSCS and NESCS, regressions of the main terms of the

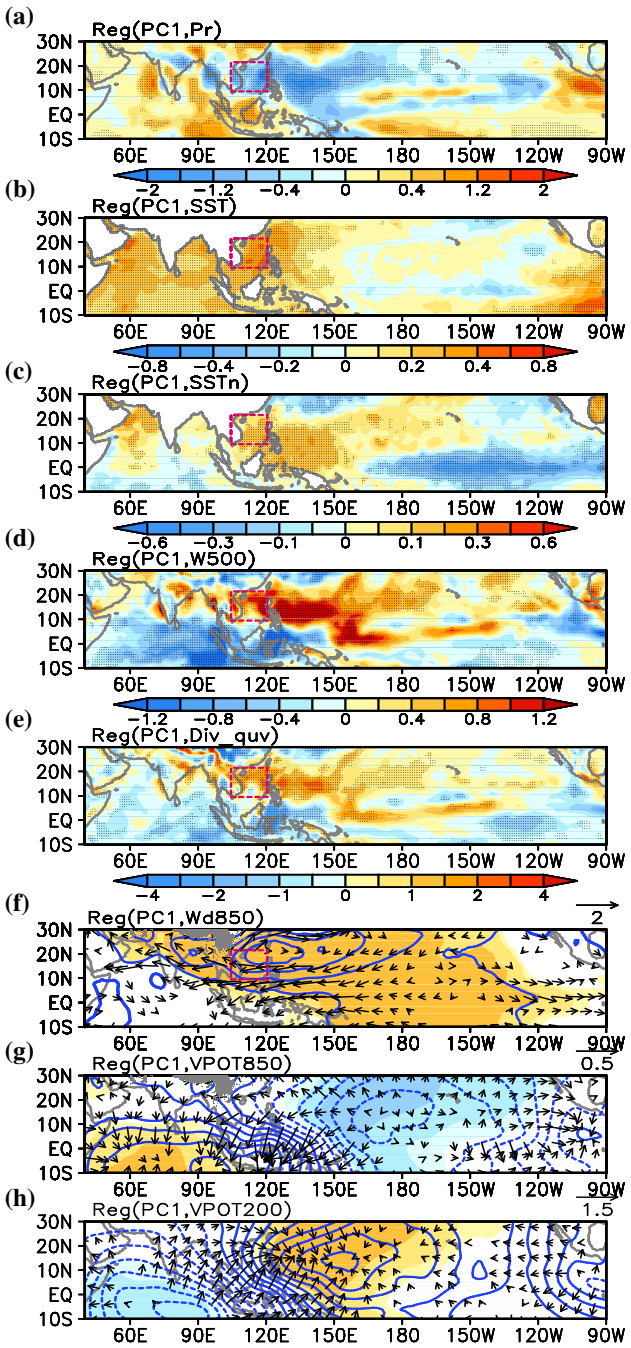

Fig. 4 Simultaneous regression with respect to the normalized first PC of the combined EOF with precipitation and SST for the period 1979–1998. **a** precipitation (mm/day), **b** SST (°C), **c** SST tendency (°C/month), **d** 500 hPa p-vertical velocity (10^{-2} Pa/s), **e** vertical integral divergence of water vapor from sea surface to 300 hPa (10^{-6} kg/m^{2}s), **f** 850 hPa winds (m/s) and geopotential height (gpm), velocity potential (contour) at 850 hPa (**g**) and 200 hPa (**h**) and the corresponding divergent winds (vectors). SST data is obtained from HadISST. Contour intervals are 2 gpm, 10^5 s^{-1}, and 2×10^5 s^{-1}in (**f**–**h**), respectively. The dots (**a**–**e**) and shading (**f**–**h**) indicate regression coefficients that are statistically significant at the 90% confidence level

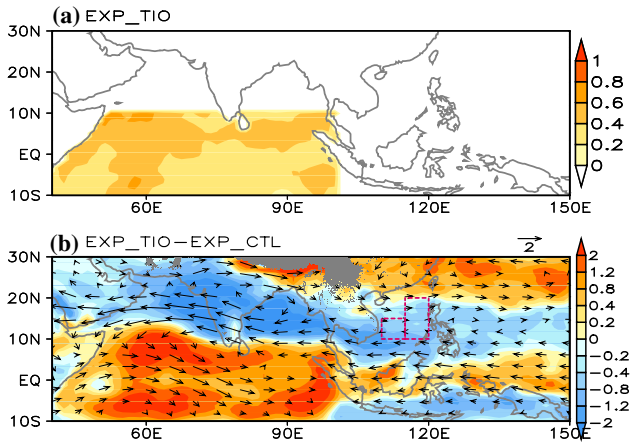

Fig. 5 a SST anomaly distribution for the tropical Indian Ocean SST experiment (EXP_TIO), b composite differences in JJA precipitation (shading, mm/day) and 850 hPa winds (vectors, m/s) between EXP_TIO and EXP_CNL

mixed-layer heat budget equation averaged over the SWSCS and NESCS onto the normalized first PC of the combined EOF during 1979–1998 are shown in Fig. 7. The mixed-layer depth is considered in the effect of surface heat flux on SST anomalies, and the units of the main terms of the heat budget equation are converted to the same units as the SST tendency (°C/month). The sum of the net surface heat flux term, heat advection, and entrainment heat flux term is slightly less than the SST tendency, which may be related to ignoring residual terms such as the effect of eddy diffusion. It can be seen that the positive anomaly of the SST tendency over the NESCS is close to that over the SWSCS during 1979–1998, whereas the NESCS displays a significant negative rainfall-SST correlation, and the negative rainfall-SST correlation in the SWSCS is weak. In the NESCS, the incoming shortwave radiation is enhanced due to suppressed convection related to below-normal rainfall, which contributes largely to the SST tendency with a shallow mixed-layer depth. The longwave radiation contribution is negative and its magnitude is about 1/5 that of the shortwave radiation. The latent heat flux has a negative contribution, with a magnitude about 1/2 that of the shortwave radiation. The anomalous northeasterly winds superimposed on the southwesterly mean winds over the SCS reduce wind speed (Fig. 6f). The effects of the enhanced sea-air humidity difference overcome the effects of decreasing surface wind speed (Fig. 6c). The evaporation in the SCS north of 12°N is obviously enhanced. The sensible heat flux and Ekman heat advection have a weakly negative contribution. The positive contributions of geostrophic heat advection and entrainment heat flux are very weak. Overall, the net surface heat flux plays a more important role in SST anomalies than oceanic processes.

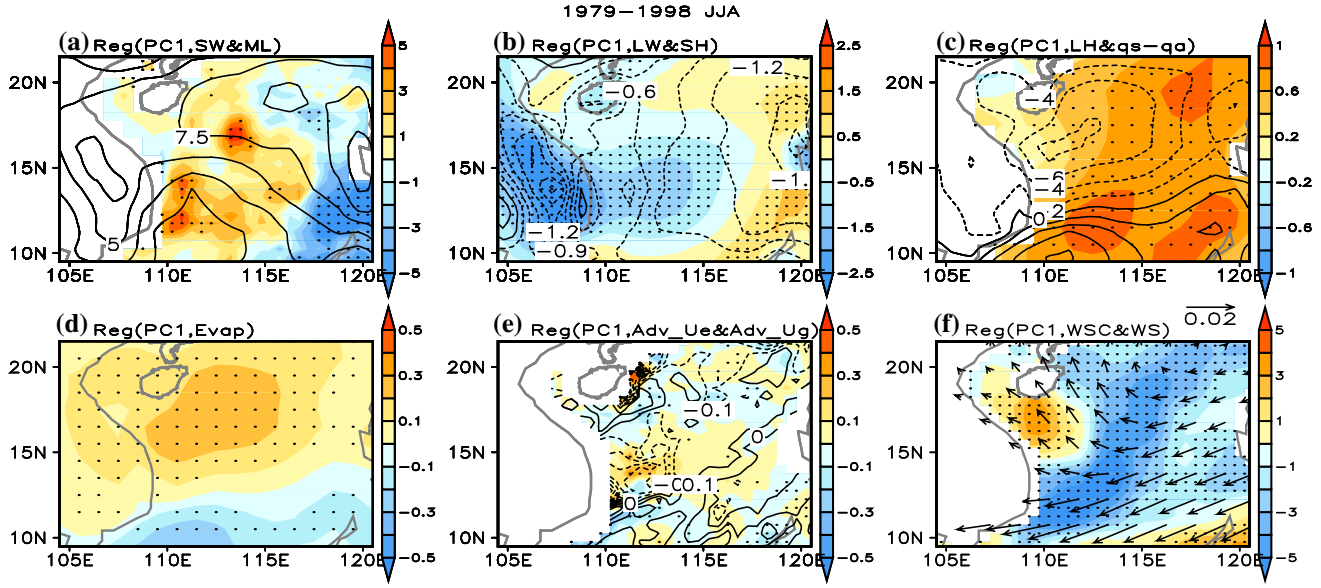

Fig. 6 Simultaneous regression with respect to the normalized first PC of the combined EOF with precipitation and SST for the period 1979–1998. **a** Shortwave radiation (contours, W/m^2), mixed-layer depth (shading, m), **b** longwave radiation (contours, W/m^2), sensible heat flux (shading, W/m^2), **c** latent heat flux (contours, W/m^2), sea-air humidity difference (shading, g/kg), **d** evaporation (shading, mm/day), **e** horizontal advection term associated with Ekman current (contours, °C/month) and geostrophic current (shading, °C/month), **f** wind stress (vectors, 10^{-8}N/m^2) and wind stress curl (shading, N/m^3). The dots indicate regression coefficients that are statistically significant at the 90% confidence level

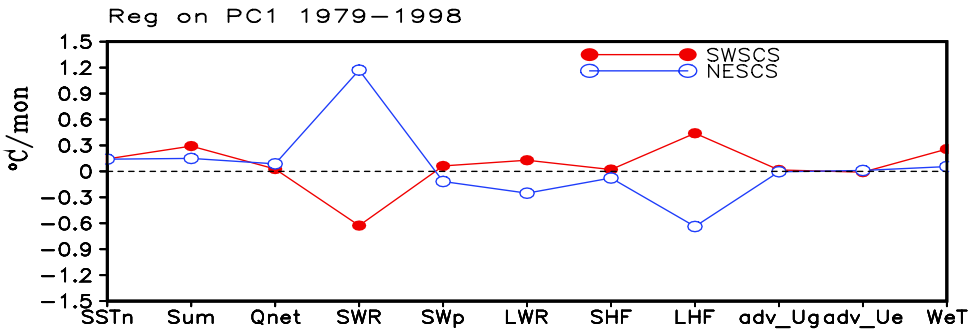

Fig. 7 Summer mixed-layer heat budget anomalies of SWSCS and NESCS (°C/month) obtained by regression onto the normalized first PC of the combined EOF with precipitation and SST for the period 1979–1998. SST tendency, net heat flux, shortwave radiation, penetrative shortwave radiation flux, longwave radiation, sensible heat flux, latent heat flux, geostrophic heat advection, Ekman heat flux, and entrainment heat flux are denoted as SSTn, Qnet, SWR,SWp, LWR, SHF, LHF, adv_Ug, adv_Ue, and WeT, respectively. The sum of Qnet, adv_Ug, adv_Ue, and WeT is denoted as Sum

In the SWSCS, entrainment heat flux contributes largely to the positive anomaly of the SST tendency, with a net surface heat flux equivalent in magnitude to that in the TropFlux dataset (figure not shown) but larger than that in the JRA-55 dataset (Fig. 7). The anomalous anticyclone corresponding to negative wind stress curl induces anomalous Ekman downwelling. Meanwhile, the coastal downwelling associated with the anomalous northeasterly winds is conducive to positive SST anomalies. Although the role of the changes in shortwave radiation, longwave radiation, and latent heat flux over the SWSCS are consistent with those over the NESCS, anomalies of surface heat flux, except for sensible heat flux, are smaller than those over the NESCS (Fig. 6). In addition, the mixed-layer depth of the SWSCS is greater than that of the NESCS, which leads to a greater modulatory effect on changes in SST. Thus, the contributions of shortwave radiation, longwave radiation, and latent heat flux to the SST tendency over the SWSCS are opposite with that over the NESCS (Fig. 7). The contributions of sensible heat flux, geostrophic heat advection, and Ekman heat advection over the SWSCS are nearly the same as those over the NESCS. Above all, the significant positive anomaly

of the SST tendency over the NESCS is determined by the net surface heat flux with an enhanced cloud-radiation effect. The positive contribution of entrainment heat flux to the SST tendency is larger than the net surface heat flux over the SWSCS.

5 Air-sea interaction over the SCS after 1999

During 1999–2013, the obvious negative relationship between local SST and precipitation can still be seen in the WNP and NESCS, which indicates atmospheric forcing of SST variation. Noticeable positive SST-precipitation relationships are present in the equatorial central-eastern Pacific, eastern Indian Ocean, Maritime Continent, and SWSCS (Fig. 8a, b), which signifies local SST forcing of atmospheric variation (Wu et al. 2006, 2013; Wu and Kirtman 2007). Negative rainfall anomalies in the WNP and NESCS are related to the negative SST anomaly in the equatorial central-eastern Pacific. This anomaly triggers an anomalous lower-level anticyclone over the SCS-WNP as a Rossby-wave response (Chen et al. 2015b), overlaid by anomalous lower-level divergence and upper-level convergence (Fig. 8g, h). It then results in anomalous descent and a negative precipitation anomaly over the SCS-WNP and anomalous ascent and a positive precipitation anomaly over the TIO. There are significant negative SST tendency anomalies over the TIO and equatorial central-eastern Pacific, whereas their corresponding rainfall anomalies are opposite. The magnitude of SST tendency anomalies in the TIO is larger than the SST anomalies. In the equatorial central eastern Pacific the magnitude of SST tendency anomalies is slightly smaller than the SST anomalies. Except for the influence of the equatorial central-eastern Pacific SST anomaly, there is another remote SST forcing that reduces SCS-WNP rainfall.

The local warmer SST anomalies from the eastern Indian Ocean to the SWSCS induce anomalous ascending motion corresponding to anomalous lower-level convergence and upper-level divergence, which acts in concert with water vapour convergence and leads to an increase in precipitation. Positive SST anomalies in the southeastern Indian Ocean-Maritime Continent could suppress convection and reduce rainfall over the SCS and WNP via meridional vertical circulation (Wu et al. 2012; He and Wu 2014; Chen et al. 2016), the influence of which exists in the two periods. The analyses above show that remote SST forcing plays a crucial role in NESCS rainfall for the whole period and in SWSCS rainfall for the period 1979–1998. During 1999–2013, local SST forcing is larger than the remote effect on SWSCS rainfall, which is the major cause of the positive SST-precipitation relationship. The magnitude of the negative SST-precipitation relationship over the NESCS decreases after 1999, which is attributed to the larger contribution of the TIO before 1999 than of the tropical central-eastern Pacific (TCEP) to NESCS rainfall after 1999, as demonstrated in Fig. 9. From the difference in 850 hPa winds and rainfall between EXP_TCEP and EXP_CNL, it can be seen that there are negative rainfall anomalies and an anomalous anticyclone over the SCS and WNP, which is due to the influence of cooler SST over the TCEP. The magnitude of rainfall and circulation over the SCS forced by the TIO is far greater than that forced by the TCEP (Fig. 5). This result is in agreement with a larger feedback coefficient of the TIO SST anomaly on the WNP anticyclone than of the Nino3 SST anomaly, derived from a linear inverse model (Fan et al. 2013).

The Indian Ocean dipole (IOD) develops during summer, matures during autumn and disappears during winter. From simultaneous regression of SST with respect to the normalized first PC of the combined EOF with precipitation and SST for the period 1979–1998 (Fig. 4b) and 1999–2013 (Fig. 8b), it shows remarkable positive TIO anomalies during 1979–1998 and very weak warming SST over TIO during 1999–2013. Thus, the simultaneous influence of IOD on the SCS summer climate is negligible.

The processes of anomalous circulation and precipitation giving feedback to the underlying SST over the NESCS and air-sea interaction over the SWSCS are estimated. The spatial patterns of longwave radiation, sensible heat flux, and latent heat flux anomalies during 1999–2013 (Fig. 10) are similar to corresponding anomalies during 1979–1998 (Fig. 6). Northeasterly wind anomalies are present in the SCS, when summer mean southwesterly winds prevail, which leads to a decrease in wind speed. Enhanced air-sea temperature and humidity differences (figure not shown) result in a decrease in the input of sensible heat flux and latent heat flux into the ocean. An increase in surface evaporation anomalies is determined by an enhanced air-sea temperature difference, but not for reduced surface wind speed. The distribution of shortwave radiation anomalies is quite different from that in the period 1979–1998, due to the change in atmospheric stability. During 1999–2013, positive anomalies of atmospheric stability are seen over the SWSCS, whereas negative anomalies are present over the NESCS. These are favourable for enhancing convection over the SWSCS and suppressing convection over the NESCS. Together with the anomalous moisture convergence in the SWSCS and the anomalous moisture divergence in the NESCS, the anomalous rainfall pattern shows positive anomalies over the SWSCS and negative anomalies over the NESCS. That causes a decrease in incoming shortwave radiation over the SWSCS and an increase over the NESCS. Precipitation over the SWSCS is enhanced in response to positive anomalies of SST, while a decrease in precipitation over the NESCS contributes positive SST anomalies. The

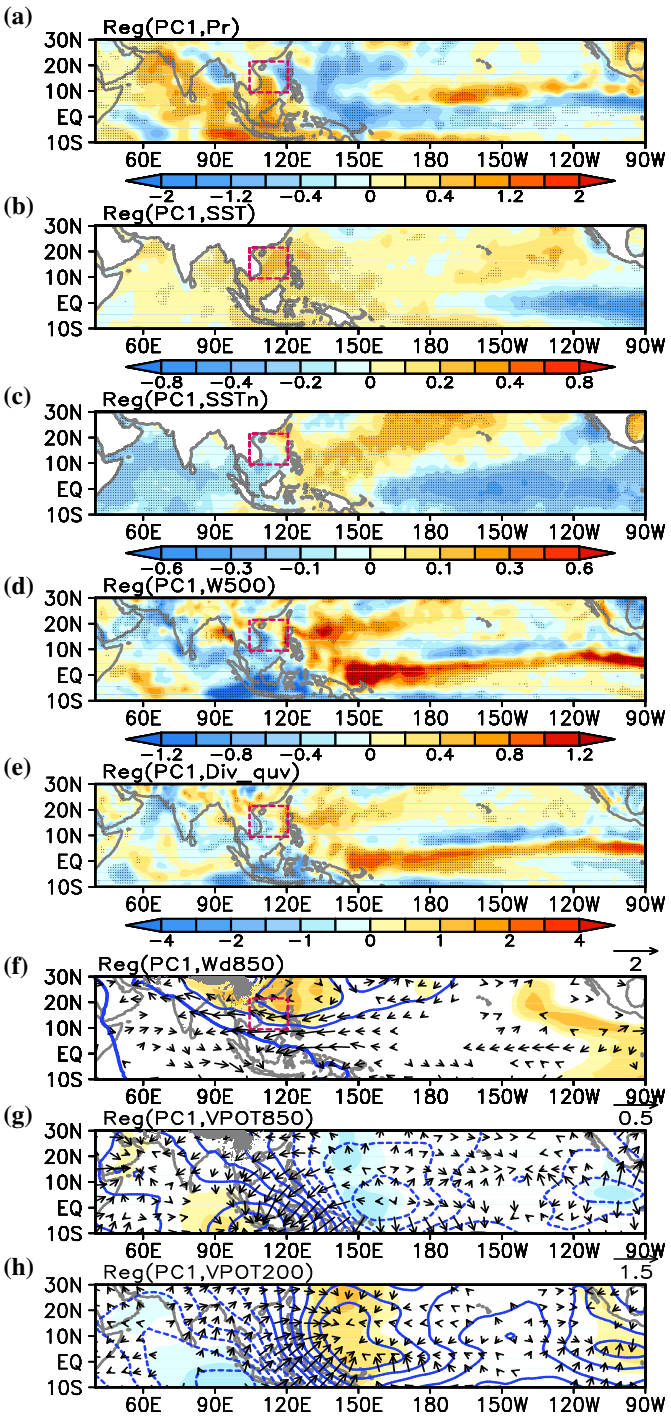

Fig. 8 Simultaneous regression with respect to the normalized first PC of the combined EOF with precipitation and SST for the period 1999–2013. **a** precipitation (mm/day), **b** SST (℃), **c** SST tendency (℃/month), **d** 500 hPa p-vertical velocity (10^{-2} Pa/s), **e** divergence of vertically integrated water vapor from sea surface to 300 hPa (10^{-6} kg/m^{2}s), **f** 850 hPa winds (m/s) and geopotential height (gpm), velocity potential at 850 hPa (**g**) and 200 hPa (**h**) and the corresponding divergent winds. Contour intervals are 2 gpm, $10^5 s^{-1}$, and 2×10^5 s^{-1}in (**f**–**h**), respectively. The dots (**a**–**e**) and shading (**f**–**h**) indicate regression coefficients that are statistically significant at the 90% confidence level

variation in the depth of the mixed layer, heat advection, and entrainment heat flux resembles that during 1979–1998. This indicates that oceanic processes make similar contributions to the SST tendency.

Figure 11 shows the regression of the mixed-layer heat budget terms averaged over the SWSCS and NESCS onto the normalized first PC for the period 1999–2013. As expected, the contribution of heat advections induced by the Ekman flow and geostrophic flow approximates that during 1979–1998. In the NESCS, the suppressed precipitation in association with a locally anomalous lower-level anticyclone and reduced cloudiness enhances incoming shortwave radiation. The magnitude of the shortwave radiation anomaly is largest, followed by the latent heat flux. The penetrative shortwave radiation flux, longwave radiation, sensible heat flux, and latent heat flux act as damping terms. The incoming shortwave radiation anomaly during 1999–2013 decreases by more than 30% in comparison with that during

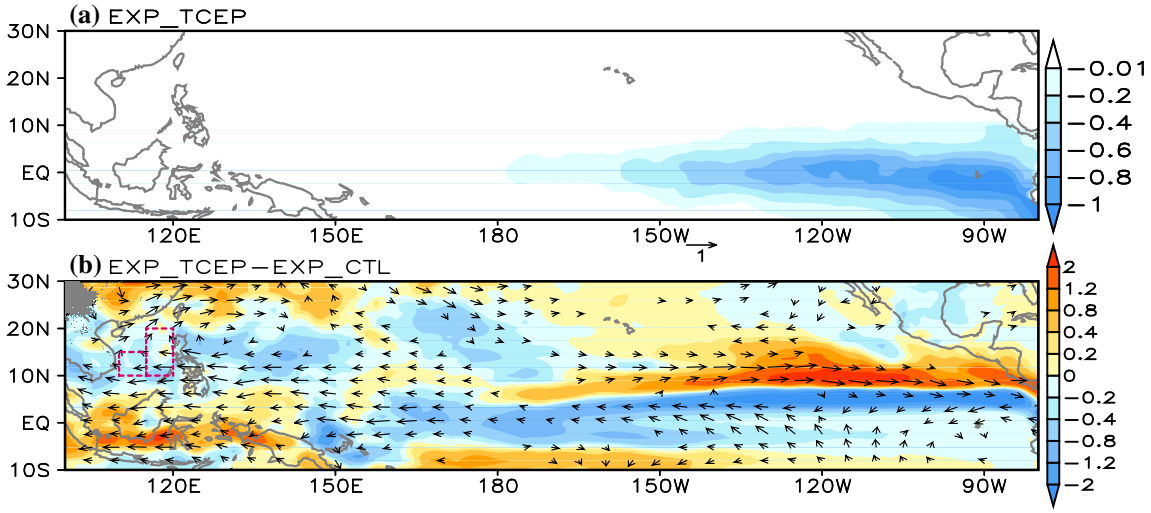

Fig. 9 **a** SST anomaly distribution for the tropical central-eastern Pacific SST experiment (EXP_TCEP), **b** composite differences in JJA precipitation (shading, mm/day) and 850 hPa winds (vectors, m/s) between EXP_TCEP and EXP_CNL

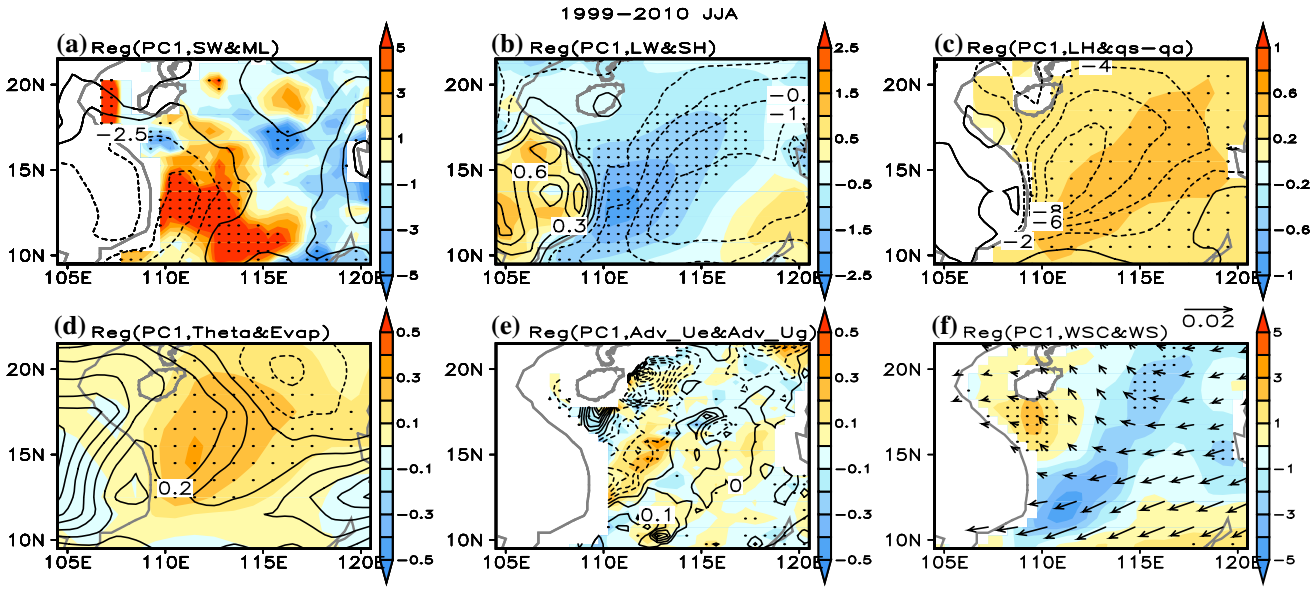

Fig. 10 Simultaneous regression with respect to the normalized first PC of the combined EOF with precipitation and SST for the period 1999–2010. **a** Shortwave radiation (contours, W/m^2), mixed-layer depth (shading, m), **b** longwave radiation (contours, W/m^2), sensible heat flux (shading, W/m^2), **c** latent heat flux (contours, W/m^2), sea-air humidity difference (shading, g/kg), **d** stability parameter (contours, K), evaporation (shading, mm/day), **e** horizontal advection term associated with Ekman current (contours, °C/month) and geostrophic current (shading, °C/month), **f** wind stress (vectors, 10^{-8}N/m^2) and wind stress curl (shading, N/m^3). The dots indicate regression coefficients that are statistically significant at the 90% confidence level

1979–1998, as the anomalous lower-level anticyclonic circulation weakens. The net surface heat flux still makes a dominant contribution to the change of SST tendency. The positive anomaly of the SST tendency experiences a substantial decrease after 1999. This means that atmospheric forcing becomes weaker corresponding to a decrease in the SST-precipitation correlation from 1979–1998 to 1999–2013.

As for the SWSCS, the anomalous surface northeasterly winds get weaker and result in the contribution of entrainment heat flux being slightly less than that during 1979–1998. Note that the magnitudes of shortwave radiation and latent heat flux have increased by about 2 times during 1999–2013. The magnitude of the positive anomaly of entrainment heat flux is nearly equivalent with the negative net surface heat flux anomaly. The local warmer SST induces

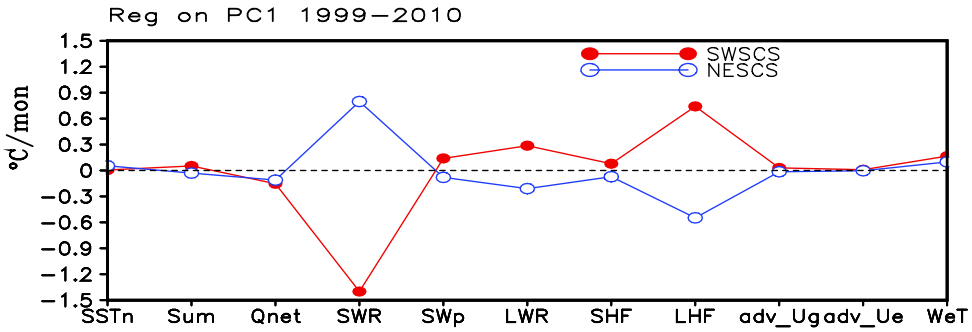

Fig. 11 Summer mixed-layer heat budget anomalies (°C/month) over the SWSCS (red line with solid circles) and NESCS (blue line with empty circles) obtained by regression on the normalized first PC of the combined EOF with precipitation and SST for the period 1999–2010

an increase in rainfall by modulating atmospheric stability and the vertical integral of water vapour flux. Negative cloud-radiation feedback does not help to maintain warmer SST. A switch from atmospheric forcing during 1979–1998 to oceanic forcing with negative cloud-radiation during 1999–2013 is identified.

6 Possible reasons for the interdecadal change in remote SST forcing

The interdecadal change in the air-sea interaction over the SCS may be associated with the interdecadal decrease in the intensity of remote SST forcing after the late 1990s. SST anomalies over the TIO and TCEP have an alternating influence on an anomalous anticyclone over the SCS-WNP during 1979–1998 and 1999–2013, respectively. This is possibly related to the evolution of TCEP SST in preceding winter. Here, we show anomalies of the 3-month moving mean SST from the preceding DJF to JJA over the TIO (50°–100°E, 10°S–10°N), Niño3 (150°–90°W, 5°S–5°N), Niño4 (160°E–150°W, 5°S–5°N), and Niño3.4 (170°–120°W, 5°S–5°N), obtained by regression on PC1 of the combined EOF in 1979–1998 and 1999–2013 (Fig. 12). During 1979–1998, the Niño3 SST anomaly in the preceding DJF is significantly positive and is larger than the Niño4 SST anomaly. The SST anomalies over Niño3, Niño4, and Niño3.4 gradually decrease from the preceding DJF to JJA, like the decaying phase of conventional El Niño. However, the positive SST anomaly over the TIO shows a slow increase, which is consistent with previous studies (e.g., Xie et al. 2009; Yuan and Yang 2012; Ren et al. 2016). The TIO SST warming induced by El Niño acts like a capacitor, sustaining atmospheric circulation after El Niño dissipates in spring (Xie et al. 2009). In JJA, when the warmer SST anomalies over Niño4 and Niño3.4 disappear, the SST anomaly over Niño3 remains positive and warmer SST anomalies over the TIO are still significant. Ren et al. (2016) indicated that significant warmer (colder) SST anomalies over the TIO can persist from spring into summer in later-decay El Niño (La Niña), which mainly results from ENSO-induced atmospheric-bridge-related processes.

During 1999–2013, TIO basin-wide SST warm condition persists from the preceding winter to spring, associated with warmer SST anomalies over the equatorial central-eastern Pacific. SST anomalies from the preceding winter to spring over the equatorial central-eastern Pacific show changes similar to those during 1979–1998, except that the magnitude of the SST anomaly over Niño4 is larger than that over Niño3 in the preceding winter. What is more, the Niño3 SST anomaly becomes significantly negative in summer, which is like the transition to a conventional La Niña from a central Pacific El Niño in the preceding winter. Due to the rapid decay of equatorial central Pacific SST anomalies, TIO basin-wide SST anomalies weaken significantly in summer. Yuan and Yang (2012) suggested that TIO SST is influenced more weakly by a central Pacific El Niño than by a conventional El Niño and has a negligible impact on the evolution of the WNP anticyclone. The evolution of the intensity of TIO SST variability is detected by moving the standard deviation of the TIO SST within a 13-year window. The intensity of TIO SST variability gets noticeably weaker after 1999 than before 1999 (Fig. 12c). This indicates a weaker remote forcing of TIO SST anomalies after 1999 than before 1999. Chen et al. (2015b) demonstrated through a suite of numerical experiments that equatorial central-eastern Pacific cooling made a major contribution to the WNP anticyclone via a Rossby wave response during La Niña developing summers. That means that summer TIO SST anomalies exert a dominant effect on the WNP anticyclone before the late 1990s, but the impacts of summer equatorial central-eastern Pacific SST anomalies become major after the late 1990s.

Previous researches had indicated IOD could influence East Asia summer monsoon in the following year (Yuan et al. 2008; Yang et al. 2010; Zhao et al. 2011). According to the method proposed by Saji et al. (1999) and Ashok et al. (2004), the IOD index is defined as SST anomaly difference between the western (60°–80°E, 10°S–10°N) and eastern (90°–110°E, 10°S–Equator) Indian Ocean. There is highly positive regression coefficient of IOD and its two poles in preceding autumn onto the normalized first PC of

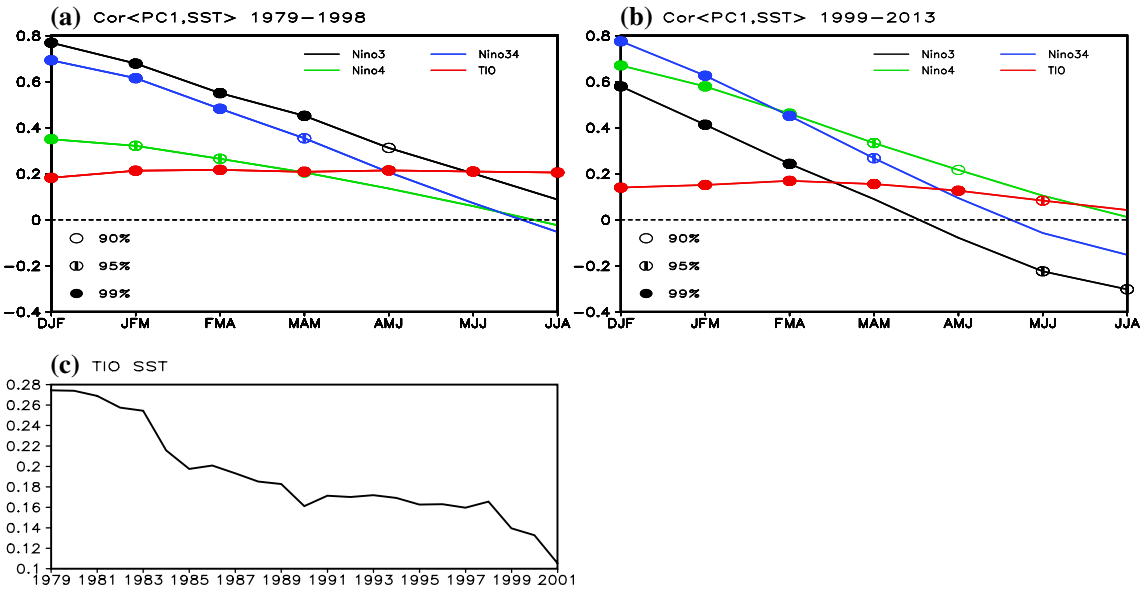

Fig. 12 SST anomalies (°C) over the TIO (10°S–10°N and 50°–100°E, red line), Niño3 (black line), Niño4 (green line), and Niño3.4 (blue line) from the preceding winter to summer obtained by regression onto the normalized first PC of the combined EOF with precipitation and SST during 1979–1998 (**a**) and 1999–2010 (**b**). Empty circles, empty circles with bars, and solid circles indicate SST anomalies that are statistically significant at the 90, 95, and 99% confidence levels, respectively. **c** The 13-year running standard deviation of JJA SST over the TIO. The standard deviation is shown for the first year of the 13-year window

the combined EOF with precipitation and SST over the SCS in summer during 1979–1998, whereas during 1999–2013 the SST anomalies of IOD and its two poles in peak season related to first PC of the combined EOF is much weaker and less significant than the previous period, especially in the eastern pole of IOD (figure not shown). That implies the impact of IOD in preceding autumn on summer SCS circulation during 1979–1998 is stronger than the later period.

The different evolutions of equatorial central-eastern Pacific SST anomalies from the preceding winter to summer associated with PC1 of the combined EOF between rainfall and SST over the SCS before and after the late1990s are possibly related to the phase transition of the PDO. Figure 13 shows that there is a closer relation between the PDO and equatorial central-eastern Pacific SST in winter during the cold phase (1999–2013) than during the warm phase (1979–1998), which is consistent with previous studies (Yeo et al. 2012; Jo et al. 2015). Jo et al. (2015) ascribed the strengthened relationship of the SST variability between the tropical Pacific and the North Pacific across the 1998/1999 regime shift to a westward shift in tropical convective heating around the dateline. However, from spring to summer, the regression coefficient of Niño3 SST onto the preceding winter PDO is significantly positive and increases obviously during 1979–1998, whereas the regression coefficient is nearly zero during 1999–2013. This implies that equatorial central-eastern Pacific SST variability in spring and summer is superimposed by the effect of the preceding winter PDO before the late 1990s, which may lead to a slow decay of equatorial central-eastern Pacific SST anomalies from the preceding winter to summer. The important impact of the preceding winter PDO on summer climatic variability has been revealed in previous studies. The winter PDO could modulate the relationship between the ENSO-related East Asian winter monsoon and the following summer monsoon (Chen et al. 2013). The winter PDO exerts a crucial influence on early summer monsoon rainfall over south China through modifying the intensity of the western Pacific subtropical high together with the effect of ENSO (Chan and Zhou 2005).

There is significant warming trend in the Indian Ocean SST throughout the past half century (Rao et al. 2012; Hiroaki et al. 2015), especially in the western tropical Indian Ocean (Roxy et al. 2014). The Indian Ocean warming can induces a decrease of rainfall over the western North Pacific with anomalous anticyclonic circulation, while salient rainfall increase in the western North Pacific is caused by the La Niña-like pattern with warmer SST over tropical western Pacific and cooler SST over tropical central-eastern Pacific. The contribution of the tropical Pacific SST to the western North Pacific rainfall is greater than the contribution of the Indian Ocean SST, demonstrated by sensitivity experiments of atmospheric general circulation model (Hiroaki et al. 2015). Around early 1990s IOD experience interdecadal change from negative phase to positive phase (Ashok et al. 2004). Yuan et al. (2008) pointed out positive (negative)

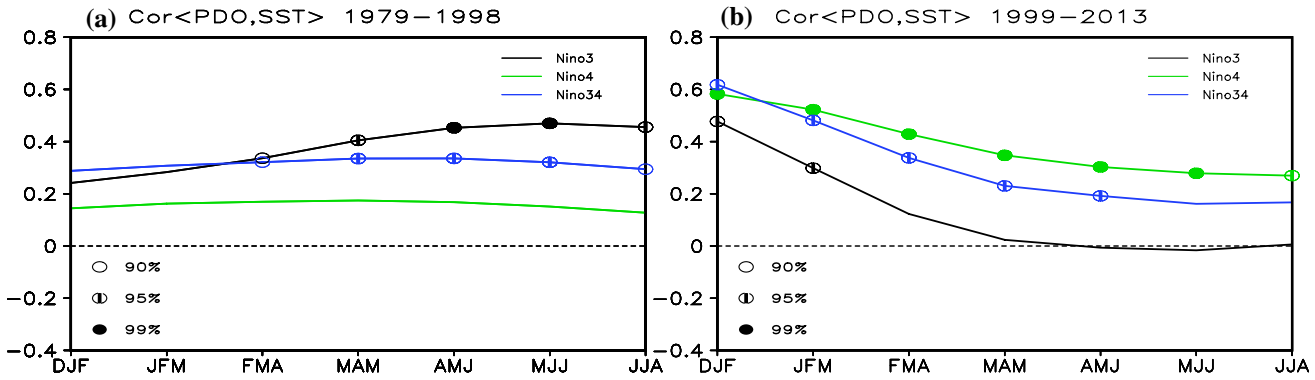

Fig. 13 SST anomalies (°C) over Niño3 (black line), Niño4 (green line), and Niño3.4 (blue line) from winter to the subsequent summer obtained by regression on the normalized winter PDO index during 1979–1998 (**a**) and 1999–2010 (**b**). Empty circles, empty circles with bars, and solid circles indicate SST anomalies that are statistically significant at the 90, 95, and 99% confidence levels, respectively

IOD could enhance (weaken) summer western pacific subtropical high in the following year. After 1999, the tropical Pacific Ocean summer SST with warmer SST over tropical western Pacific and cooler SST over tropical central-eastern Pacific enhances summer SCS rainfall (Hiroaki et al. 2015). That means interdecadal effect of tropical Pacific Ocean summer SST offsets the IOD effect in peak season in some extent after 1999.

7 Summary and discussion

The local simultaneous precipitation-SST and precipitation-SST tendency correlations show interdecadal change in the air–sea interaction over the SCS after 1999, which is associated with the changes of local SST threshold for deep convection and remote SST forcing. Over the NESCS, the precipitation-SST correlation experiences an interdecadal decrease around the late 1990s. During 1979–1998, the precipitation-SST correlation is significantly negative, corresponding to the negative precipitation-SST tendency correlation. The anomalous anticyclone and reduced rainfall over the SCS-WNP are ascribed primarily to remote forcing from positive SST anomalies over the TIO (Fig. 14a). Suppressed convection and cloudlessness promote an increase in incoming shortwave radiation and contribute the most to the positive SST tendency. In contrast, during 1999–2013 the precipitation-SST and precipitation-SST tendency correlation over the NESCS is still negative, but its magnitude is reduced, which is related to the change in remote SST forcing. The TCEP SST anomalies trigger an anomalous anticyclone over the SCS-WNP accompanied by suppressed convection, which contributes to the positive SST tendency through the cloud-radiation effect (Fig. 14b). The influence of TCEP SST anomalies on circulation and rainfall variations over the SCS is much weaker than that of TIO SST anomalies, as demonstrated by numerical sensitivity experiments.

Over the SWSCS, there is a weakly negative precipitation-SST relationship during 1979–1998, while during 1999–2008 the precipitation-SST correlation becomes significantly positive. In the period 1979–1998, under the influence of TIO SST anomaly, the magnitude of anomalous downward net shortwave radiation is smaller and the anomalous mixed-layer depth increases in comparison with that over the NESCS. The net shortwave radiation provides a negative contribution to the positive SST tendency. The anomalous lower-level anticyclone induces anomalous Ekman downwelling and the northeasterly anomaly arouses coastal downwelling, which makes entrainment heat flux a more important contributor to the SST tendency. The contribution of oceanic dynamic over the SWSCS is larger than that over the NESCS. Thus, this leads to negative precipitation-SST and precipitation-SST tendency relationships over the SWSCS during 1979–1998. During 1999–2013, the local SST forcing over the SWSCS overcomes the remote forcing from SST anomalies over the TCEP and southeastern Indian Ocean-Maritime Continent. An increase in SWSCS rainfall as a response to a positive local SST anomaly (Fig. 14b), associated with enhanced convection, has a negative cloud-radiation feedback on the SST anomaly. Thus, the precipitation-SST correlation is of opposite sign to the precipitation-SST tendency correlation. For the whole period, the anomalous northeasterly winds reduce surface mean southwesterly winds, so an increase in evaporation depends on the difference in air-sea temperature. The wind-evaporation feedback does not work over the NESCS and SWSCS.

The remote forcing of the TIO SST anomaly on SCS rainfall and circulation weakens after the late 1990s, and thus the local SST forcing of the SWSCS SST anomaly can be identified clearly. That may be attributed to the decay of equatorial central-eastern Pacific SST anomalies from the

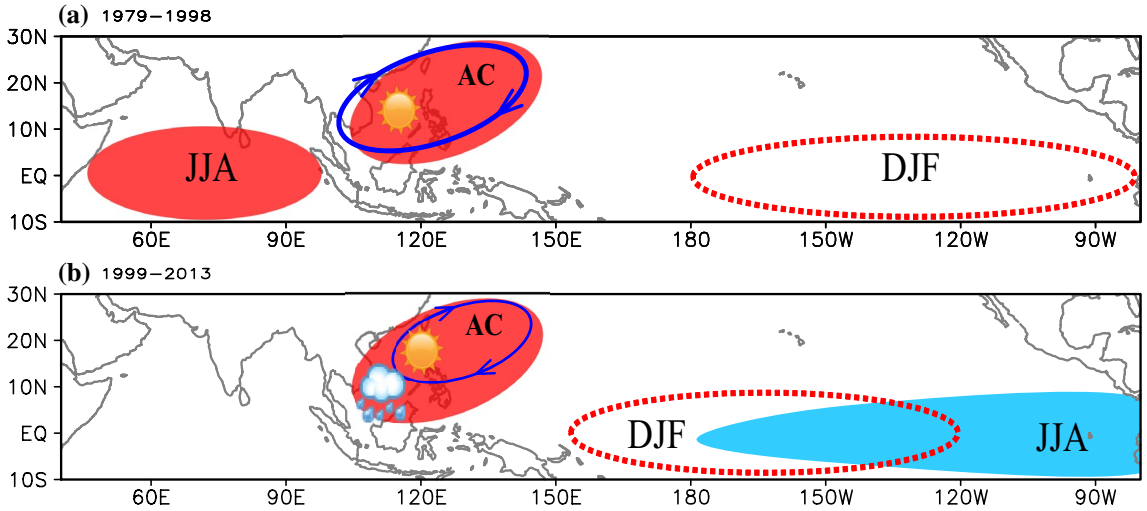

Fig. 14 Schematic diagrams summarizing the possible reasons for the interdecadal change of SST-precipitation relationship over SCS. Dashed red lines represent the anomalously warmer SST anomalies in preceding winter. Solid lines with arrows denote anomalous western North Pacific anticyclone (AC). Red and blue shadings indicate anomalously warmer and cooler SST anomalies in summer, respectively

preceding winter to summer, associated with the phase transition of the PDO (Fig. 14). During the warm phase of the PDO, the winter PDO is likely favourable for late decay of equatorial central Pacific SST anomalies from winter to the subsequent summer. This study looked for further insight into the air-sea interaction over the SCS in summer and may provide benefits for regional and global models in reproducing atmospheric and oceanic circulations. Otherwise, there is a cold filament over the SWSCS in summer (Xie et al. 2003). An increase in SWSCS SST may provide a favorable condition for tropical cyclones to form in or enter the SCS. Chen et al. (2012) suggested that the increase in summer tropical cyclones formed in the SCS is related to warmer local SST. Kajikawa and Wang (2012) also indicated that a significant increase in SST over the equatorial western Pacific enhanced tropical cyclone activity over the SCS and Philippine Sea from mid-April to mid-May. The contribution of tropical cyclone–induced rainfall associated with warmer SST over the SWSCS to local total rainfall will be investigated in the next paper.

Previous researches indicate there is multi-timescale air-sea interactions over tropical Ocean. The air–sea interactions on subseasonal time scale have been explored in the Indian Ocean (Fu and Wang 2004; Rajendran et al. 2004), the Arabian Sea, the Bay of Bengal (Roxy et al. 2013), and SCS (Roxy and Tanimoto 2012; Ye and Wu 2015) in summer. Interannual air-sea interactions exhibit obvious seasonality and regionality over tropical Ocean (Wu and Kirtman 2007; He and Wu 2013). This study emphasizes the summer air-sea interaction over the SCS experiences interdecadal change around late 1990s. Quasi-biweekly oscillation and 30–50-day oscillation as two major types of atmospheric intraseasonal oscillations over the SCS during boreal summer, their intensity changes are primarily linked with the equatorial central and eastern Pacific SST anomalies and the western Indian Ocean SST anomalies, respectively (Yang et al. 2008). Whether ocean–atmosphere coupling progresses in 10–20- and 30–50-day intraseasonal oscillations contribute the interdecadal change of the air-sea interaction over the SCS is an interesting subject in future studies.

Acknowledgements This research was jointly supported by the Strategic Priority Research Program of the Chinese Academy of Sciences (Grant no. XDA11010403), the CAS/SAFEA International Partnership Program for Creative Research Teams, the National Natural Science Foundation of China (Grant nos. 41506004, 41521005, 41422601, 41376025, 41675062, 41530530, and 41506003), the Guangdong Natural Science Foundation (no. 2016A030310113), and the project of Guy Carpenter Asia-Pacific Climate Impact Centre (no. 9360126). ZW acknowledges the support of National Key Basic Research and Development Projects of China (2016YFA0600601). The authors gratefully acknowledge the use of the HPCC for all numeric simulations and data analysis at the South China Sea Institute of Oceanology, Chinese Academy of Sciences.

References

Adler RF, Huffman GJ, Chang A, Ferraro R, Xie P, Janowiak J, Rudolf B, Schneider U, Curtis S, Bolvin D, Gruber A, Susskind J, Arkin P (2003) The Version 2 Global Precipitation Climatology Project (GPCP) Monthly precipitation analysis (1979-Present). J Hydrometeor 4:1147–1167

Ashok K, Chan WL, Motoi T, Yamagata T (2004) Decadal variability of the Indian Ocean dipole. Geophys Res Lett 31 (24): L24207. https://doi.org/10.1029/2004GL021345

Chan JCL, Zhou W (2005) PDO, ENSO and the early summer monsoon rainfall over south China. Geophys Res Lett 32(8):93–114
Chen JP, Wu RG, Wen ZP (2012) Contribution of South China Sea tropical cyclones to an increase in southern China summer rainfall around 1993. Adv Atmos Sci 29(3):585–598
Chen W, Feng J, Wu RG (2013) Roles of ENSO and PDO in the link of the East Asian Winter Monsoon to the following summer monsoon. J Clim 26(2):622–635
Chen JP, Wen ZP, Wu RG, Chen ZS, Zhao P (2014a) Interdecadal changes in the relationship between SC winter-spring precipitation and ENSO. Clim Dyn 43:1327–1338
Chen ZS, Wen ZP, Wu RG, Zhao P, Cao J (2014b) Influence of two types of El Niño on the East Asian climate during boreal summer: a numerical study. Clim Dyn 43:1–13
Chen ZS, Wen ZP, Wu RG, Lin XB, Wang JB (2015a) Relative importance of tropical SST anomalies in maintaining the western North Pacific anomalous anticyclone during El Niño to La Niña transition years. Clim Dyn 46:1027–1041
Chen JP, Wen ZP, Wu RG, Chen ZS, Zhao P (2015b) Influences of northward propagating 25–90-day and quasi-biweekly oscillations on eastern China summer rainfall. Clim Dyn 45:105–124
Chen JP, Wen ZP, Wu RG, Wang X, He C, Chen ZS (2016) An interdecadal change in the intensity of interannual variability in summer rainfall over southern China around early 1990s. Clim Dyn 48:191–207
Dong SF, Gille ST, Sprintall J (2007) An assessment of the Southern Ocean mixed layer heat budget. J Clim 20:4425–4442
Fan L, Shin SI, Liu QY, Liu ZY (2013) Relative importance of tropical SST anomalies in forcing East Asian summer monsoon circulation. Geophys Res Lett 40:2471–2477
Fu X, Wang B (2004) The Boreal-Summer Intraseasonal Oscillations Simulated in a Hybrid Coupled Atmosphere Ocean Model. Mon Weather Rev 132(132):2628–2649
Gadgil S, Joseph PV, Joshi NV (1984) Ocean-atmosphere coupling over monsoon regions. Nature 312:141–143
Graham NE, Barnett TP (1987) Sea surface temperature, surface wind divergence, and convection over tropical oceans. Science 238:657–659
Groves DG, Hunt LM (1980) Ocean World Encyclopedia. McGraw-Hill Book Company, pp 356–358
He ZQ, Wu RG (2013) Seasonality of interannual atmosphere–ocean interaction in the South China Sea. J Oceanogr 69(6):699–712
He ZQ, Wu RG (2014) Indo-Pacific remote forcing in summer rainfall variability over the South China Sea. Clim Dyn 42:2323–2337
He B, Yang S, Li ZN (2016) Role of atmospheric heating over the South China Sea and western Pacific regions in modulating Asian summer climate under the global warming background. Clim Dyn 46:2897–2908
Hiroaki U, Youichi K, Masamitsu H et al (2015) Combined effects of recent Pacific cooling and Indian Ocean warming on the Asian monsoon. Nat Commun 6:8854
Hu C, Lee Z, Franz BA (2012) Chlorophyll-a algorithms for oligotrophic oceans: A novel approach based on three-band reflectance difference. J Geophys Res 117:C01011. https://doi.org/10.1029/2011JC007395
Jo HS, Yeh SW, Lee SK (2015) Changes in the relationship in the SST variability between the tropical Pacific and the North Pacific across the 1998/1999 regime shift. Geophys Res Lett 42. https://doi.org/10.1002/2015GL065049
Johnson NC, Xie SP (2010) Changes in the sea surface temperature threshold for tropical convection. Nat Geosci 3:842–845
Kajikawa Y, Wang B (2012) Interdecadal change of the South China Sea summer monsoon onset. J Clim 25:3207–3218
Kobayashi S, Ota Y, Harada Y, Ebita A, Moriya M, Onoda H, Onogi K, Kamahori H, Kobayashi C, Endo H, Miyaoka K, Takahashi K (2015) The JRA-55 Reanalysis: General specifications and basic characteristics. J Meteor Soc Jpn 93:5–48
Kumar BP, Vialard J, Lengaigne M, Murty VSN, McPhaden MJ (2012) TropFlux: Air-sea fluxes for the global tropical oceans-description and evaluation. Clim Dyn 38:1521–1543
Kumar A, Chen M, Wang W (2013) Understanding prediction skill of seasonal mean precipitation over the tropics. J Clim 26:5674–5681
Lau NC, Nath MJ (2009) A model investigation of the role of air-sea interaction in the climatological evolution and ENSO-related variability of the summer monsoon over the South China Sea and western North Pacific. J Clim 22(18):35–41
Levitus S (1982) Climatological Atlas of the World Ocean, vol 173. NOAA Professional Paper 13, US Department of Commerce, pp 962–963
Li XZ, Wen ZP, Zhou W (2011) Long-term change in summer water vapor transport over south China in recent decades. J Meteor Soc Jpn 89A:271–282
Li XZ, Zhou W, Chen DL, Li CY, Song J (2014) Water vapor transport and moisture budget over Eastern China: Remote forcing from the two types of El Niño. J Clim 27:8778–8792
Liang JY, Wen ZP, Chen JP, Wu LJ (2013) The characteristics of tropical sea surface temperature anomalies and related influences on the onset of South China Sea summer monsoon. Atmos Ocean Sci Lett 6(5):266–272
Lindzen RS, Nigam N (1987) On the role of sea surface temperature gradients in forcing low-level winds and convergence in the tropics. J Atmos Sci 44:2418–2436
Liu S, Duan A (2017) Impacts of the leading modes of tropical indian ocean sea surface temperature anomaly on sub-seasonal evolution of the circulation and rainfall over East Asia during boreal spring and summer. J Meteor Res 31(1):171–186
Lu RY, Lu S (2014) Local and remote factors affecting the SST–precipitation relationship over the western North Pacific during summer. J Clim 27(13):5132–5147
Morel A (1988) Optical modeling of the upper ocean in relation to its biogenous matter content (case I waters). J Geophys Res 93(C9):10749–10768
Neal R, Chen C et al. (2012) Description of the NCAR community atmosphere model (CAM 5.0). NCAR Technical NoteTN-486
Paulson CA, Simpson JJ (1977) Irradiance measurements in the upper ocean. J Phys Oceanogr 7:952–956
Rajendran K, Kitoh A, Arakawa O (2004) Monsoon low-frequency intraseasonal oscillation and ocean-atmosphere coupling over the Indian Ocean. Geophys Res Lett 31:L02210. https://doi.org/10.1029/2003GL019031
Rajendran K, Nanjundiah RS, Gadgil S, Srinivasan J (2012) How good are the simulations of tropical sst–rainfall relationship by ipcc ar4 atmospheric and coupled models? J Earth Syst Sci 121(3):595–610
Rao SA, Dhakate AR, Saha SK et al (2012) Why is Indian Ocean warming consistently? Clim Change 110(3–4):709–719
Rayner NA, Parker DE, Horton EB, Folland CK, Alexander LV, Rowell DP, Kent EC, Kaplan A (2003) A global analysis of sea surface temperature, sea ice, and night marine air temperature since the late nineteenth century. J Geophys Res 108(D14):4407
Ren RC, Sun SY, Yang Y, Li Q (2016) Summer SST anomalies in the Indian Ocean and the seasonal timing of ENSO decay phase. Clim Dyn 47(5–6):1827–1844
Reynolds RW, Smith TM, Liu C, Chelton DB, Casey KS, Schlax MG (2007) Daily high-resolution-blended analyses for sea surface temperature. J Clim 20:5473–5496
Roxy M, Tanimoto Y (2012) Influence of sea surface temperature on the intraseasonal variability of the South China Sea summer monsoon. Clim Dyn 39:1209–1218

Roxy M, Tanimoto Y, Preethi B, Terray P, Krishnan R (2013) Intraseasonal SST-precipitation relationship and its spatial variability over the tropical summer monsoon region. Clim Dyn 41(1):45–61

Roxy M, Ritika K, Terray P, Masson S (2014) The curious case of Indian Ocean Warming. J Clim 27(22):8501–8509

Saji NH, Goswami BN, Vinayachandran PN, Yamagata T (1999) A dipole mode in the Tropical Indian Ocean. Nature 401:360–363

Smith T, Reynolds R, Peterson T, Lawrimore J (2008) Improvements to NOAA's historical merged land–ocean surface temperature analysis (1880–2006). J Clim 21:2283–2296

Song W, Lan J, Liu QY, Sui DD, Zeng LL, Wang DX (2014) Decadal variability of heat content in the South China Sea inferred from observation data and an ocean data assimilation product. Ocean Sci 10:135–139

Thangaprakash VP, Girishkumar MS, Suprit K et al (2016) What controls seasonal evolution of sea surface temperature in the Bay of Bengal? Mixed layer heat budget analysis using moored Buoy observations Along 90°E. Oceanography 29(2):202–213

Wang B, Zhang Q (2002) Pacific-East Asian teleconnection part II: How the Philippine Sea anomalous anticyclone is established during El Niño development. J Clim 15:3252–3265

Wang B, Ding QH, Fu XH, Kang IS, Jin K, Shukla J, Doblas-Reyes F (2005) Fundamental challenge in simulation and prediction of summer monsoon rainfall. Geophys Res Lett 32(15):291–310

Wang CZ, Wang WQ, Wang DX, Wang Q (2006) Interannual variability of the South China Sea associated with El Niño. J Geophys Res 111:C03023

Wang B, Huang F, Wu Z, Wu ZW, Yang J, Fu XH, Kikuchi K (2009) Multi-scale climate variability of the South China Sea monsoon: A review. Dyn Atmos Oceans 47:15–37

Wang GH, Wang CZ, Huang RX (2010) Interdecadal variability of the eastward current in the South China Sea associated with the summer Asian monsoon. J Clim 23(22):6115–6123

Wu R (2002) Processes for the northeastward advance of the summer monsoon over the Western North Pacific. J Meteor Soc Jpn 80(1):67–83

Wu RG, Kirtman BP (2007) Regimes of local air-sea interactions and implications for performance of forced simulations. Clim Dyn 29:393–410

Wu RG, Wang B (2001) Multi-stage onset of the summer monsoon over the western North Pacific. Clim Dyn 17(4):277–289

Wu RG, Kirtman BP, Pegion K (2006) Local air–sea relationship in observations and model simulations. J Clim 19:4914–4932

Wu B, Zhou TJ, Li T (2009) Contrast of rainfall-SST relationships in the western North Pacific between the ENSO-developing and ENSO-decaying summers. J Clim 22(16):4398–4405

Wu RG, Wen ZP, Yang S, Li YQ (2010) An interdecadal change in southern China summer rainfall around 1992/93. J Clim 23:2389–2403

Wu RG, Yang S, Wen ZP, Huang G, Hu KM (2012) Interdecadal change in the relationship of southern China summer rainfall with tropical Indo-Pacific SST. Theor Appl Climatol 108(1):119–133

Wu RG, Chen JP, Wen ZP (2013) Precipitation–surface temperature relationship in the IPCC CMIP5 models. Adv Atmos Sci 30(3):766–778

Xie PP, Arkin PA (1997) Global precipitation: a 17-year monthly analysis based on gauge observations, satellite estimates, and numerical model outputs. Bull Amer Meteor Soc 78:2539–2558

Xie SP, Xie Q, Wang DX, Liu WT (2003) Summer upwelling in the South China Sea and its role in regional climate variations. J Geophys Res 108(C8):3261. https://doi.org/10.1029/2003JC001867

Xie SP, Hu KM, Hafner J, Tokinaga H, Du Y, Huang G, Sampe T (2009) Indian Ocean capacitor effect on Indo–western Pacific climate during the summer following El Niño. J Clim 22:730–747

Yang J, Wang B, Wang B (2008) Anticorrelated intensity change of the quasi-biweekly and 30–50 day oscillations over the South China Sea. Geophys Res Lett 35:L16702. https://doi.org/10.1029/2008GL034449

Yang JL, Liu QY, Liu ZY (2010) Linking observations of the Asian monsoon to the Indian Ocean SST: possible roles of Indian Ocean Basin mode and dipole mode. J Climate 23(21):5889–5902

Ye KH, Wu RG (2015) Contrast of local air–sea relationships between 10–20-day and 30–60-day intraseasonal oscillations during May–September over the South China Sea and western North Pacific. Clim Dyn 45:3441–3459

Yeo SR, Kim KY, Yeh SW, Kim WM (2012) Decadal changes in the relationship between the tropical Pacific and the North Pacific. J Geophys Res Atmos 117(D15). https://doi.org/10.1029/2012JD017775

Yuan Y, Yang S (2012) Impacts of different types of El Niño on the East Asian climate: Focus on ENSO cycles. J Clim 25(21):7702–7722

Yuan Y, Yang H, Zhou W, Li C (2008) Influences of the indian ocean dipole on the asian summer monsoon in the following year. Int J Climatol 28(14):1849–1859

Zhang ZX, Zhang Q, Chen X, Zhang JC, Zhou JW (2011) Statistical properties of moisture transport in East Asia and their impacts on wetness/dryness variations in north China. Theor Appl Climatol 104(3):337–347

Zhao S, Zhou T, Yang X, Zhu Y, Tan Y, Sun X (2011) Interdecadal change of the relationship between the tropical indian ocean dipole mode and the summer climate anomaly in china. Acta Meteorol Sin 25(2):129–141

Zhou TJ, Yu RC (2005) Atmospheric water vapor transport associated with typical anomalous summer rainfall patterns in China. J Geophys Res Atmos 110:D08104. https://doi.org/10.1029/2004JD005413

Zhu YL, Wang HJ, Zhou W, Ma JH (2011) Recent changes in the summer precipitation pattern in East China and the background circulation. Clim Dyn 36:1463–1473

Zhu YL, Wang HJ, Ma JH, Wang T, Sun JQ (2015) Contribution of the phase transition of Pacific Decadal Oscillation to the late 1990s' shift in East China summer rainfall. J Geophys Res Atmos 120:8817–8827